

Upscaling acoustic wave equation using renormalization group theory

Ajay Malkoti¹, Shravan M. Hanasoge², and René-Édouard Plessix³

ABSTRACT

Seismic waves interact with a broad range of heterogeneities as they propagate through the earth. Simulating this full range of scales for wave propagation requires capturing heterogeneities of all scales, which can be computationally unaffordable. In such cases, we have relied on macroscopic representations of media obtained through an upscaling process that preserves the effects of small-scale heterogeneities (in comparison with the wavelengths of interest). Here, we discuss the application of the renormalization group (RG) theory-based upscaling to the 2D acoustic wave equation. RG-based upscaling requires constructing a special Fourier operator and is implemented using a domain decomposition in conjunction with an “expansion and truncation” method to mitigate edge effects. We test this upscaling method on several benchmark models and in the context of reverse time migration. The upscaled models obtained using this method indicate a good consistency for generated waveforms, whereas the runtime for simulations is reduced by at least an order of magnitude.

INTRODUCTION

Seismic imaging techniques, such as reverse time migration (RTM), least-squares RTM, or full-waveform inversion, require the simulation of wave propagation inside an idealized earth. Wave propagation is sensitive to earth’s parameter variations inside a Fresnel volume (Spetzler and Snieder, 2004) due to the finite-frequency nature of the seismic experiment. Numerically, we cannot account for all scales of the heterogeneities because it would be computationally very expensive. Therefore, we work with a macroscopic representation of the earth’s parameters. When we discretize

the wave equation using a numerical scheme, e.g., a finite-difference method, the representation of the solution and model parameters are generally dictated by the cell size or grid spacing because we associate material parameter(s), e.g., velocities and density, with each cell. Grid spacing is typically defined in terms of a fraction of the (minimum) wavelength to limit the numerical dispersion of the scheme (Dablain, 1986). As a general rule, second-, fourth-, and eighth-order schemes require approximately 16, 8, and 4 grid nodes per wavelength, respectively. The grid cannot capture variations in heterogeneities smaller than the spacing, although waves in real media are sensitive to them up to a certain extent. Thus, it is very useful to determine the best-possible macroscopic values for subgrid-scale heterogeneities on the grid. Effective medium (Backus, 1962; Schoenberg and Muir, 1989) or homogenization theory (Bensoussan et al., 1978) tells us how to define these macroscopic parameters. Effective or coarse representations of fine-scale model variations may have reduced symmetry, i.e., they contain extrinsic/layered anisotropy. In other words, a fine-scale layered isotropic medium is well described by an effective coarse-scale anisotropic medium (e.g., Backus, 1962). However, this also depends on the structure of the wave equation; for example, upscaling the acoustic wave speed in the simple acoustic wave equation does not result in lowered symmetry, as we will see in the forthcoming sections. There are a range of different upscaling methods, each based on a variety of assumptions because there are no optimal choices for the approximations. Without being exhaustive, we cite operator-based upscaling (Christie, 1996; Vdovina et al., 2005), the averaging of displacement-stress, displacement-energy, or stress-energy relations (Zijl et al., 2002; Grechka and Kachanov, 2006; Gao et al., 2015), homogenization theory (Moulinec and Suquet, 1998; Brisard and Dormieux, 2010; Cance and Capdeville, 2015; Capdeville et al., 2015; Burgos et al., 2016; Mishra et al., 2016; Song and Jordan, 2018), wavelet-based theory (Dorobantu and Engquist, 1998; Andersson et al., 1999; Persson and Runborg, 2001; Chertock and Levy, 2005; Coulth, 2006; Engstrom and Sjoberg, 2007; De Leon,

Manuscript received by the Editor 20 September 2021; revised manuscript received 20 January 2022; published ahead of production 29 March 2022; published online 9 May 2022.

¹Tata Institute of Fundamental Research, Colaba, Mumbai, India and CSIR-National Geophysical Research Institute, Habsiguda, Hyderabad, India. E-mail: ajaymalkoti@ngri.res.in (corresponding author).

²Tata Institute of Fundamental Research, Colaba, Mumbai, India. E-mail: hanasoge@tifr.res.in.

³Shell Global Solutions International B.V., Amsterdam, The Netherlands. E-mail: reneedouard.plessix@shell.com.

© 2022 Society of Exploration Geophysicists. All rights reserved.

2008; Engquist and Runborg, 2009), and renormalization group (RG)-based theory (Hanasoge, 2016; Fichtner and Hanasoge, 2017; Hanasoge et al., 2017; Kennett and Fichtner, 2020). Those efforts have shown that even if one limits the analysis to the acoustic wave propagation, the effective upscaled “acoustic” macroscopic parameters include the effects of some small-scale variations that can be of elastic nature. Here, we discuss an efficient implementation of RG theory with the acoustic wave equation.

RG theory aims at correcting the wave equation parameters in such a way that the simulated waveform still includes the effects of the small-scale variations, despite a coarse discretization. In this method, the low-wavenumber part of the given model parameters, which can be adequately sampled by a coarse grid, is modified to account for the effects caused by the high-wavenumber variations that are only visible on a fine grid. RG theory-based upscaling requires multidimensional forward and inverse Fourier transforms to go back and forth between the spatial and wavenumber domains and involves inverting a large matrix when applied on the full computational domain (Hanasoge, 2016; Fichtner and Hanasoge, 2017). In realistic numerical applications, this can lead to a large computational overhead. In this work, we propose the RG-upscaling method based on modified Fourier operator and domain decomposition. We divide the complete domain into several subdomains to reduce the computational overhead and to allow for the possibility of a parallel implementation. However, a straightforward application of this upscaling in each subdomain leads to edge effects caused by artificial discontinuities between the subdomains. We then implement an expansion and truncation technique that allows overlapping between neighboring subdomains and thus avoids those edge effects. This method differs from the overlapping domain decomposition technique.

The outline of the paper is as follows. In the first part, we apply RG theory to the 2D acoustic wave equation using modified Fourier operator. In the second part, we explain how the entire domain is decomposed into subdomains and how expansion and truncation technique is applied for upscaling. Subsequently, we describe some numerical examples to evaluate the proposed approach, followed by a summary and conclusions.

THEORY

We begin with the acoustic wave equation in the frequency (temporal Fourier) domain:

$$-\omega^2 p(\omega, \mathbf{x}) = c^2(\mathbf{x}) \Delta p(\omega, \mathbf{x}) + s(\omega, \mathbf{x}), \quad (1)$$

where p and s are the pressure field and the source function, respectively; Δ is the Laplace operator; \mathbf{x} is the spatial coordinate; ω is the angular frequency; and c is the acoustic or compressional velocity.

The product $q(\omega, \mathbf{x}) = c^2(\mathbf{x}) \Delta p(\omega, \mathbf{x})$ between the model parameter $c(\mathbf{x})$ and the Laplacian of the pressure field $\Delta p(\omega, \mathbf{x})$ in the spatial domain becomes a convolution in the wavenumber (spatial Fourier) domain. Indeed, $\hat{q}(\omega, \mathbf{k}) = \int_{-\infty}^{\infty} \mathbf{k}^2 \hat{p}(\omega, \mathbf{k}) c^2(\mathbf{k}' - \mathbf{k}) d\mathbf{k}'$, where \mathbf{k} denotes the wavenumber and the quantities with and without a hat sign are in the wavenumber domain and spatial domain, respectively. This convolution means that all the wavenumbers of the model parameter c^2 affect the pressure wave’s propagation up to a certain extent depending on the smoothness of the parameter’s variations with respect to the wavelength. Therefore, one cannot fully isolate the response corresponding to only the low wavenumbers, i.e., the smooth component of the model parameter. Even when we are interested only

in the low-frequency response, we theoretically need to solve the wave equation with a complete wavenumber representation of the seismic parameters, i.e., over a fine grid that captures the full range of parameter variations. In practice, this would be computationally very expensive. A typical remedy consists of calculating effective macroscopic parameters, whereas limiting errors arise from coarse-grid discretization.

To achieve this, we transform the wave equation (equation 1) into the wavenumber domain by applying the spatial Fourier operator \mathcal{F} (see Appendix A). Because the Fourier operator is invertible ($\mathcal{F}^{-1}\mathcal{F} = \mathcal{F}\mathcal{F}^{-1} = I$, with I being the identity operator), we may rewrite equation 1 as follows:

$$-\omega^2 \mathcal{F}^{-1} \mathcal{F} p = \mathcal{F}^{-1} \mathcal{F} c^2 \mathcal{F}^{-1} \mathcal{F} \Delta \mathcal{F}^{-1} \mathcal{F} p + \mathcal{F}^{-1} \mathcal{F} s. \quad (2)$$

We now define the following quantities in the wavenumber domain:

$$\begin{cases} \hat{p} = \mathcal{F} p \\ \hat{s} = \mathcal{F} s \\ \hat{C} = \mathcal{F} c^2 \mathcal{F}^{-1} \\ \hat{\Delta} = \mathcal{F} \Delta \mathcal{F}^{-1} \end{cases} \quad (3)$$

Multiplying equation 2 by \mathcal{F} , we obtain the wavenumber-domain acoustic wave equation:

$$-\omega^2 \hat{p} = \hat{C} \hat{\Delta} \hat{p} + \hat{s}. \quad (4)$$

Given an arbitrary user-prescribed, case-specific, cut-off wavenumber, we may decompose the spatial Fourier operator into two parts \mathcal{F}_l and \mathcal{F}_h , yielding the low- and high-wavenumber parts, respectively (see Appendix A). In this manner, pressure and source terms can be written as, respectively,

$$\hat{p} = \begin{pmatrix} \hat{p}_l \\ \hat{p}_h \end{pmatrix} = \begin{pmatrix} \mathcal{F}_l p \\ \mathcal{F}_h p \end{pmatrix}, \quad \hat{s} = \begin{pmatrix} \hat{s}_l \\ \hat{s}_h \end{pmatrix} = \begin{pmatrix} \mathcal{F}_l s \\ \mathcal{F}_h s \end{pmatrix}, \quad (5)$$

where the operator containing the parameters \hat{C} is

$$\begin{aligned} \hat{C} &= \begin{pmatrix} \mathcal{F}_l \\ \mathcal{F}_h \end{pmatrix} c^2 \begin{pmatrix} \mathcal{F}_l^{-1} & \mathcal{F}_h^{-1} \end{pmatrix} = \begin{pmatrix} \mathcal{F}_l c^2 \mathcal{F}_l^{-1} & \mathcal{F}_l c^2 \mathcal{F}_h^{-1} \\ \mathcal{F}_h c^2 \mathcal{F}_l^{-1} & \mathcal{F}_h c^2 \mathcal{F}_h^{-1} \end{pmatrix} \\ &= \begin{pmatrix} \hat{C}_{ll} & \hat{C}_{lh} \\ \hat{C}_{hl} & \hat{C}_{hh} \end{pmatrix}, \end{aligned} \quad (6)$$

and the derivative operator $\hat{\Delta}$ is

$$\hat{\Delta} = \begin{pmatrix} \mathcal{F}_l \\ \mathcal{F}_h \end{pmatrix} \Delta \begin{pmatrix} \mathcal{F}_l^{-1} & \mathcal{F}_h^{-1} \end{pmatrix} = \begin{pmatrix} \hat{\Delta}_{ll} & 0 \\ 0 & \hat{\Delta}_{hh} \end{pmatrix}. \quad (7)$$

With these definitions, we obtain the following system of equations governing \hat{p}_l and \hat{p}_h :

$$\begin{cases} -\omega^2 \hat{p}_l = \hat{C}_{ll} \hat{\Delta}_{ll} \hat{p}_l + \hat{C}_{lh} \hat{\Delta}_{hh} \hat{p}_h + \hat{s}_l \\ -\omega^2 \hat{p}_h = \hat{C}_{hl} \hat{\Delta}_{ll} \hat{p}_l + \hat{C}_{hh} \hat{\Delta}_{hh} \hat{p}_h + \hat{s}_h \end{cases} \quad (8)$$

Equations for \hat{p}_l and \hat{p}_h are coupled, as expected, because the spatial-domain product between model parameters and derivatives of the pressure correspond to a convolution in the wavenumber (spatial Fourier) domain. The second part of equation 8 gives

$$\hat{p}_h = -(\omega^2 + \hat{C}_{hh}\hat{\Delta}_{hh})^{-1}\hat{C}_{hl}\hat{\Delta}_{ll}\hat{p}_l - (\omega^2 + \hat{C}_{hh}\hat{\Delta}_{hh})^{-1}\hat{s}_h. \quad (9)$$

Using this expression to eliminate \hat{p}_h in the first part of equation 8, we arrive at the equation for the pressure field in the low-wavenumber regime \hat{p}_l :

$$\begin{aligned} -\omega^2\hat{p}_l &= [\hat{C}_{ll} - \hat{C}_{lh}\hat{\Delta}_{hh}(\omega^2 + \hat{C}_{hh}\hat{\Delta}_{hh})^{-1}\hat{C}_{hl}]\hat{\Delta}_{ll}\hat{p}_l \\ &\quad + \hat{s}_l - \hat{C}_{lh}\hat{\Delta}_{hh}(\omega^2 + \hat{C}_{hh}\hat{\Delta}_{hh})^{-1}\hat{s}_h. \end{aligned} \quad (10)$$

Defining

$$\begin{cases} \hat{C}_E(\omega) = [\hat{C}_{ll} - \hat{C}_{lh}\hat{\Delta}_{hh}(\omega^2 + \hat{C}_{hh}\hat{\Delta}_{hh})^{-1}\hat{C}_{hl}], \\ \hat{s}_E(\omega) = \hat{s}_l - \hat{C}_{lh}\hat{\Delta}_{hh}(\omega^2 + \hat{C}_{hh}\hat{\Delta}_{hh})^{-1}\hat{s}_h \end{cases}, \quad (11)$$

we obtain the following equation for \hat{p}_l :

$$-\omega^2\hat{p}_l = \hat{C}_E(\omega)\hat{\Delta}_{ll}\hat{p}_l + \hat{s}_E(\omega). \quad (12)$$

To transform equation 12 back to the spatial domain, we first rewrite it by equating the identity with the product of the Fourier with its inverse:

$$\begin{aligned} -\omega^2\mathcal{F}_l\mathcal{F}_l^{-1}\hat{p}_l &= \mathcal{F}_l\mathcal{F}_l^{-1}\hat{C}_E(\omega)\mathcal{F}_l\mathcal{F}_l^{-1}\hat{\Delta}_{ll}\mathcal{F}_l\mathcal{F}_l^{-1}\hat{p}_l \\ &\quad + \mathcal{F}_l\mathcal{F}_l^{-1}\hat{s}_E(\omega). \end{aligned} \quad (13)$$

Then, by introducing

$$\begin{cases} C_E = \mathcal{F}_l^{-1}\hat{C}_E(\omega)\mathcal{F}_l, \\ \Delta_{ll} = \mathcal{F}_l^{-1}\hat{\Delta}_{ll}\mathcal{F}_l, \\ s_E = \mathcal{F}_l^{-1}\hat{s}_E(\omega) \end{cases}, \quad (14)$$

and multiplying equation 13 by \mathcal{F}_l^{-1} , we obtain with $p_l = \mathcal{F}_l^{-1}\hat{p}_l$:

$$-\omega^2 p_l = C_E(\omega)\Delta_{ll}p_l + s_E(\omega). \quad (15)$$

Equation 12 is not the standard wave equation because the model parameter operator \hat{C}_E depends on frequency. Thus, within this framework, upscaling leads to frequency-dependent parameters. To obtain a pure acoustic wave equation, we further simplify the approach by fixing the angular frequency in C_E and s_E to $\omega = \omega_0$. The reference angular frequency ω_0 could be a representative value within the frequency band of the seismic experiment. If we assume $\omega^2\hat{\Delta}_{hh}^{-1} \ll \hat{C}_{hh}$, we can choose $\omega_0 = 0$, and \hat{C}_E simplifies to

$$\hat{C}_E \simeq [\hat{C}_{ll} - \hat{C}_{lh}\hat{C}_{hh}^{-1}\hat{C}_{hl}]. \quad (16)$$

With this approximation, \hat{C}_E (and similarly \hat{s}_E) becomes frequency independent and equation 13 reduces to a standard acoustic wave equation. The term \hat{C}_{ll} in equation 16 represents the low-wavenumber part for the complete domain, which is equivalent to the apodization of undesired spatial wavenumbers. The remaining part $\hat{C}_{lh}\hat{C}_{hh}^{-1}\hat{C}_{hl}$, known as the correction term, arises due to the effect of high wavenumbers. With the acoustic wave equation, the low-frequency component of the Fourier-derivative operator emerges from RG theory; i.e., $\Delta_{ll} = \mathcal{F}_l^{-1}\hat{\Delta}_{ll}\mathcal{F}_l$. An important caveat is that this is

not true for general derivative operators, in which density or tensor coefficients need to be considered (Hanasoge, 2016; Fichtner and Hanasoge, 2017). Invoking scale separation and dropping the temporal-frequency dependency in the effective wave speed equation yield nearly identical results; for example, tests performed with and without constant frequency term (i.e., $\omega = 0$) in equation 12 produce the same answers for low frequencies.

NUMERICAL IMPLEMENTATION

The finite-difference solution of wave equation demands minimum numerical-dispersion error by constraining the grid spacing, $\Delta h < \lambda_{\min}/n$, where λ_{\min} is the smallest wavelength traveling in the medium and n is the number of grid points per wavelength. The numerical scheme of order $\mathcal{O}(\Delta t^2, \Delta^4)$ requires λ_{\min} to be sampled by at least eight grid nodes. These criteria are independent of the variations in the model parameters. However, a highly heterogeneous model may require sampling it with a very fine grid spacing (up to Nyquist frequency); otherwise, any high-wavenumber variations present in the model are lost. The fine sampling rate is much higher than the one prescribed by the dispersion criteria, and it results in greatly increased computational cost. This, in turn, also controls the time step (Δt) by virtue of the Courant condition. Therefore, we would like to upscale this fine-scale model to a coarser model with grid spacing as demanded by dispersion criteria or as close as possible while preserving the wave characteristics and reducing its computational cost.

Let us assume a computational domain with lengths L_x and L_z along the x - and z -directions, respectively, and discretized with uniform spacing Δh_f along both axes (Figure 1a). Here, subscript f refers to the fine-sampled model. The fine grid contains $N_{xf} \times N_{zf}$ number of nodes, where $N_{xf} = \lfloor L_x/\Delta h_f \rfloor + 1$, $N_{zf} = \lfloor L_z/\Delta h_f \rfloor + 1$, and $\lfloor \cdot \rfloor$ represents the floor function. This model can be upscaled using the proposed RG theory-based upscaling technique in several ways. The most straightforward way is to consider the entire model and upscaling it will yield the parameter model consisting of $N_{xc} \times N_{zc}$ number of nodes with a grid spacing Δh_c , (Figure 1a) and here, $N_{xc} = \lfloor L_x/\Delta h_c \rfloor + 1$ and $N_{zc} = \lfloor L_z/\Delta h_c \rfloor + 1$. This strategy is adopted by Fichtner and Hanasoge (2017) with the 1D wave equation. However, it is very challenging to extend this approach to higher dimensions because the computational cost of the scheme rises sharply with domain size because it involves storing and inverting the very large size Fourier matrix (see \hat{C}_{hh} term in equation 16). For example, for 1D domain with N nodes and 2D domain with $N \times N$ nodes, the Fourier matrices are of size N^2 and N^4 , respectively. Furthermore, the computational complexity for inverting a matrix of size $N \times N$ is given by $O(N^a)$, where $2.73 < a < 3$, depending on the algorithm used for the inversion (Coppersmith and Winograd, 1987).

To reduce the size of the Fourier transform, we first decompose the entire domain into subdomains of lengths L'_x and L'_z (described in Hanasoge et al., 2017), as shown in Figure 1b. This gives $(L_x/L'_x) \times (L_z/L'_z)$ number of subdomains. Each subdomain contains $N'_{xf} \times N'_{zf}$ number of grid nodes at the fine discretization level and $N'_{xc} \times N'_{zc}$ grid nodes at the coarse discretization level (upscaled model). Here, we require the number of nodes in the fine grid of the subdomain in each direction to be an integer multiple of the number of nodes in the coarse grid. The final RG-upscaled (URG) model is obtained by joining all upscaled subdomains. For the wave upscaling problem, we observe some edge effects in the final upscaled

parameter model, which introduces artificial discontinuities at the edges, as shown in Figure 2. Our attempts to mitigate this effect using some well-known techniques of applying a taper (e.g., Hann or Tukey window) lead to instabilities in the solver.

The edge effect can be avoided using the expansion and truncation technique with overlapping (Figure 1c). In this technique, the model is expanded with a few additional layers of nodes around the domain (to be upscaled). After upscaling the expanded domain, the additional node layers should be removed or truncated to obtain the exact upscaled subdomain. The additional node layers create an overlap region that helps in maintaining the continuity. This overlap region should be large enough to avoid the artifacts but small enough to not add appreciably to the computation cost. To begin with this method, we first choose the size of the subdomain along any axis (L'') based on the classical Rayleigh limit for resolution, which states that two events cannot be resolved by a wave if their

separation is less than a quarter of wavelength. Based on this, we can choose the size of the subdomain as $\min(L''_x, L''_z) > (\lambda_{\min}/4)$, where λ_{\min} is the smallest wavelength traveling in the medium. Then, we define the coarsening ratio or decimation level σ as the ratio of the number of nodes in a given subdomain to that of an upscaled domain. For simplicity's sake, we consider only power-of-two ratios: $\sigma_x = N''_{xf}/N''_{xc} = 2^i$ and $\sigma_z = N''_{zf}/N''_{zc} = 2^j$ (for integers i and j). Without expansion, the application of upscaling independently on each subdomain generates edge effects over q_x and q_z node layers around the edges of the subdomains, as observed in the upscaled model (Figure 2b). In the present analysis, we use $q_x = q_z = 4$ for all cases. We expand each subdomain with $p_x = \sigma_x q_x$ nodes on both sides of the x -direction and $p_z = \sigma_z q_z$ nodes on both sides of the z -direction. This means that the expanded subdomain has $(N''_{xf} + 2p_x) \times (N''_{zf} + 2p_z)$ grid nodes at the fine discretization and $(N''_{xc} + 2q_x) \times (N''_{zc} + 2q_z)$ grid nodes after upscaling with the coarse discretization. We then truncate the upscaled domain by removing the additional nodes (q_x and q_z) arising due to the expansion around the subdomain. This complete process, called expansion and truncation of subdomains, is shown in Figure 3.

The method requires some adaptations for the subdomains situated at the edges or corners of the model in which expansion in some directions is not possible. In this situation, we can artificially extend the domain with a simple extrapolation scheme or ignore the expansion in which it is not possible.

NUMERICAL RESULTS

We apply different upscaling approaches to each fine-scale reference model (called REF) to assess the relative performance of the RG theory-based method.

- Arithmetic or harmonic averaging: The model parameter on the coarse grid is obtained by averaging over the values on the fine grid $M_{kl} = \sum_{i=k\sigma_x}^{(k+1)\sigma_x-1} \sum_{j=l\sigma_z}^{(l+1)\sigma_z-1} w_{ij} m_{ij}$, where M_{kl} is the value defined on the coarse grid, m_{ij} is the material parameter to be averaged on the fine grid, and w_{ij} represents

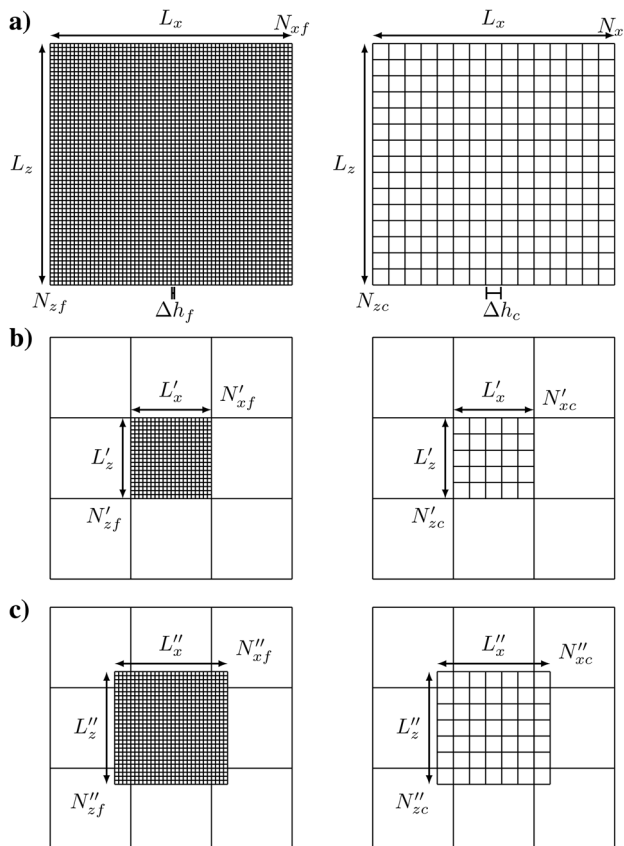


Figure 1. Upscaling the given fine-sampled model (left column) to a coarse-upscaled model (right column) using the RG theory-based technique, which is possible in three ways. The first is shown in (a) in which the complete domain is taken as such and upscaled to yield a coarse model. The second is shown in (b) in which the domain is deconstructed into several subdomains and then each subdomain is upscaled individually and independently. Subsequently, all upscaled subdomains are stitched together to yield the complete upscaled-coarse model. Third, the expansion and truncation technique is shown in (c). In this technique, the selected subdomain is first expanded with a few additional nodes and upscaled, which also contains additional nodes. The desired upscaled part is extracted by truncating the additional nodes. The additional nodes around the upscaled subdomains overlap with neighboring subdomains, which maintain the continuity.

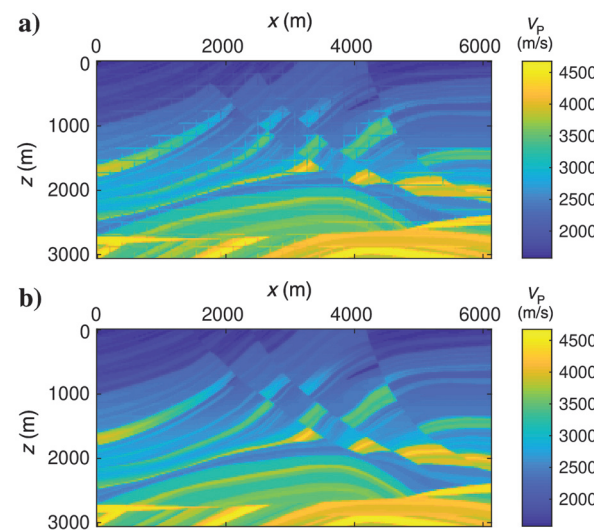


Figure 2. (a) The edge effect for the Marmousi model when it is upscaled using a block of size $N'_x \times N'_z$, each of which is directly upscaled onto a block of size $N''_x \times N''_z$. (b) The upscaled Marmousi model with the expansion and truncation technique.

the weights such that their sum is unity. In the present case, we use $w_{ij} = 1/(\sigma_x \sigma_z)$, and averaging is carried out on the inverse of wave speed because it better preserves the traveltimes. Models upscaled with this method are called “upscaled average” (UAV).

- Wavenumber-domain filtering using Gaussian window: The model parameter is transformed into the wavenumber domain and low-pass filtered using a Gaussian $w(k) = \exp(-(k^2/4D^2))$ for $|k| \leq k_0$ and 0 otherwise, where $k = \sqrt{k_x^2 + k_z^2}$ and k_x and k_z are the wavenumbers along the x - and z -directions, respectively; $k_0 = 2\pi/\lambda_0$ is the wavenumber corresponding to the user-prescribed threshold value of wavelength λ_0 ; and D is a parameter that controls the slope of the Gaussian curve. Finally, the values on the coarse grid are obtained with the inverse Fourier transform. Models upscaled using this method are called “upscaled Gaussian filtered” (UFG).
- RG theory: The parameters on the coarse grid are obtained using the approach described previously with reference angular frequency $\omega_0 = 0$. Models upscaled using this method are called “URG.”

To demonstrate the application of the RG upscaling, we will use different models (presented later in this section) and different geometries, namely, transmission and reflection geometry. These three upscaling methods will be applied to each model and compared for their performance.

Transmission geometry

In the transmission case example, we consider an REF model consisting of 1024×512 nodes. The source and receiver are located at the same depth near left ($(x, z) = d_f(42, 258)$) and right ($(x, z) = d_f(986, 258)$) edges of model, respectively. The fine grid representation corresponds to a spacing of $d_f = 1.5$ m and with an upscaling of $\sigma = 4$, and the coarse spacing is $d_c = 6$ m. Absorbing conditions are applied at all boundaries for transmission geometry. We use the broadband Ricker wavelet of central frequency f_0 , which shows a good frequency response up to $1.645f_0$ (Wang, 2015). We have performed simulations for various values of f_0 (5 Hz, 10 Hz, 15 Hz, and 20 Hz) for which the maximum frequency of response is $f_{\max} = 8.22$ Hz, 16.45 Hz, 24.67 Hz, and 32.9 Hz, respectively. For the given source-receiver distance and the average velocity of 1500 m.s $^{-1}$ (least value for all models), seismic waves propagate approximately 5 wavelengths and 31 wavelengths at central frequencies of $f_0 = 5$ and 20 Hz, respectively. The numerical wave simulation is carried out using a fourth-order finite-difference scheme with vectorization (Malkoti et al., 2018; Li et al., 2021). We note that the 6 m spacing corresponds to about one-tenth of the wavelength at 24.64 Hz (the maximum frequency of the approximate 15 Hz Ricker wavelet).

Model with random perturbations

The reference velocity model in this case is described by $c(x, z) = c_0 + \Delta c(x, z)$, where the model has a uniform background P-wave velocity

of $c_0 = 1500$ m.s $^{-1}$ and Δc is a uniform-random variable with a maximum permissible amplitude of 20% of c_0 value. In Figure 4, we show the reference (REF) and upscaled models (UAV, UFG, and URG); the value c_0 has been subtracted. The difference plot reveals that the UFG model differs least from c_0 , followed by URG and the largest deviations for the UAV model. As evident from the figure, only the UAV and URG models could preserve the high-frequency characteristics. How these characteristics in upscaled models affect the kinematic and dynamic features of the seismogram is shown in Figure 5.

The synthetic seismogram obtained for the fine-scale model is marked as a reference (REF). At the low-frequency end of our analysis, 5 Hz, all models produce nearly identical seismograms. However, as the source frequency increases (up to 15 Hz), there is an onset of traveltimes error in all cases and the error is relatively large for the UFG model. At higher frequencies, all waveforms show significant errors in amplitude and traveltime. At the highest frequencies, the performance of the RG theory-based upscaling is roughly equivalent to that of an averaging method.

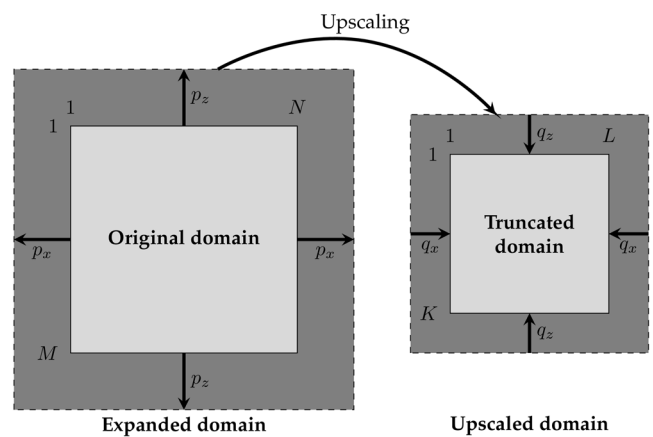


Figure 3. The expansion and truncation method. The domain is expanded along top/bottom and left/right directions by p_x and p_z numbers of nodes, respectively. After upscaling, q_x and q_z edge nodes are truncated from the upsampled domain along with vertical and horizontal directions, respectively.

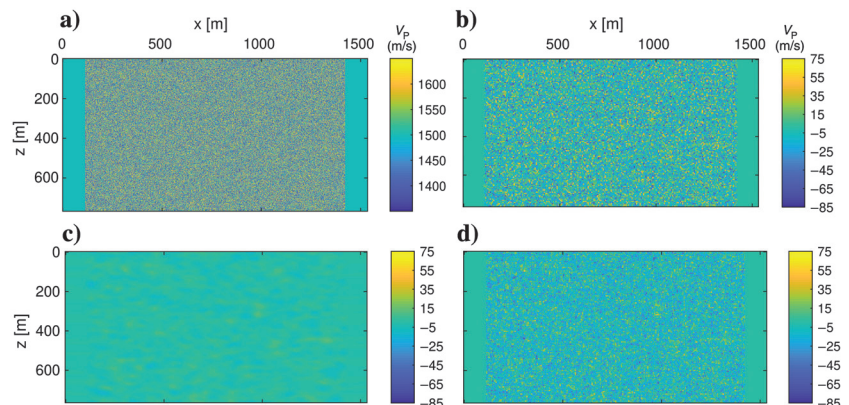


Figure 4. A comparison of the different upscaling techniques applied on random-perturbation model. The fine-scale reference model (REF) is shown in (a), and its upscaled models are shown in (b)–(d) after subtracting the background velocity $c_0 = 1500$ m.s $^{-1}$ to emphasize on the differences. (b) The UAV model, (c) UFG model, and (d) URG model.

Model with periodic perturbations

A reference periodic model (Figure 6) is generated using a checkerboard grid, where $c_0 = 1500 \text{ m.s}^{-1}$ and Δc represents periodic fluctuation between 0 and 300 m.s^{-1} with a periodicity of 3 m. The model size and the fine grid spacing are the same

Figure 5. All traces in each subplot are obtained for the random model using the same source frequency (top-left). These are compared between the reference (REF) model and upscaled models (URG, UAV, and UFG). Here, the decimation level σ represents the ratio of the number of nodes in a given subdomain to that in the upscaled domain.

as for the previous model (i.e., random model). As for the random model, we plot the REF and upscaled models with subtracted $c_0 = 1500 \text{ m.s}^{-1}$, which is related to plotting only. The upscaled medium velocity is highest for UFG, whereas the other two models, UAV and URG, are very close. The traces generated for the REF and upscaled media are shown in Figure 7. For this model as well,

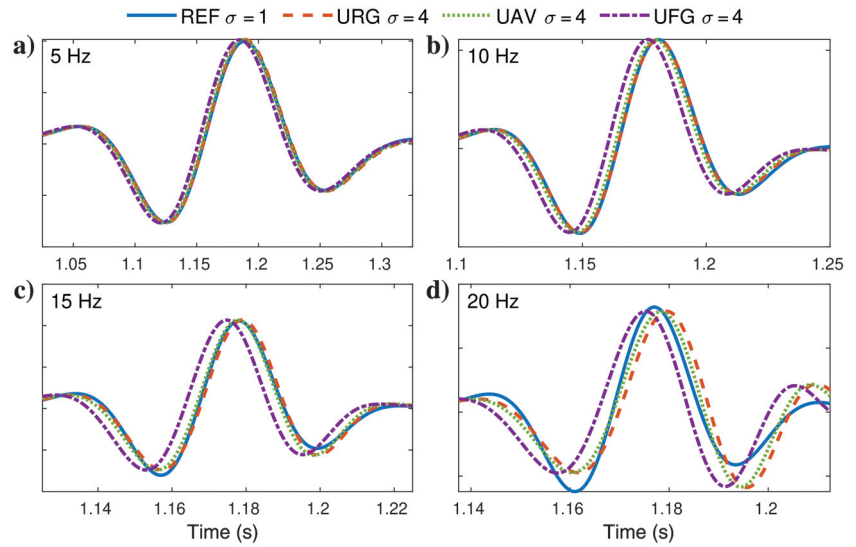


Figure 6. A comparison of different upscaling techniques applied on periodic model. The fine-scale reference model (REF) is shown in (a), and its checkerboard pattern is magnified for better visualization. The upscaled model's difference from their background velocity $c_0 = 1500 \text{ m.s}^{-1}$ is shown in each subplot: (b) the UAV model, (c) UFG model, and (d) URG model.

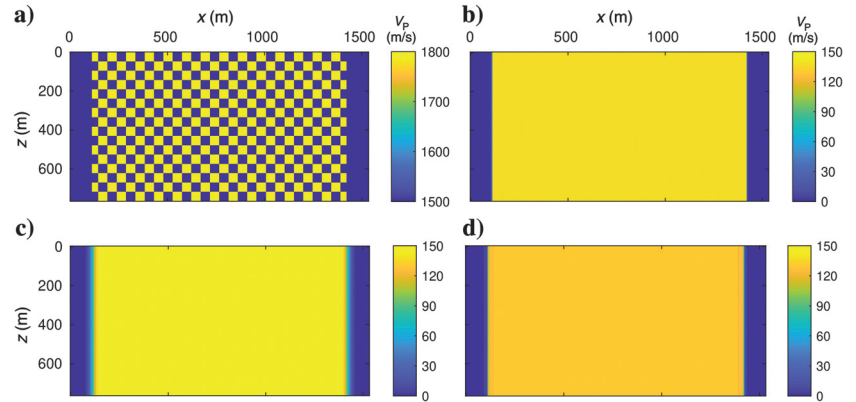
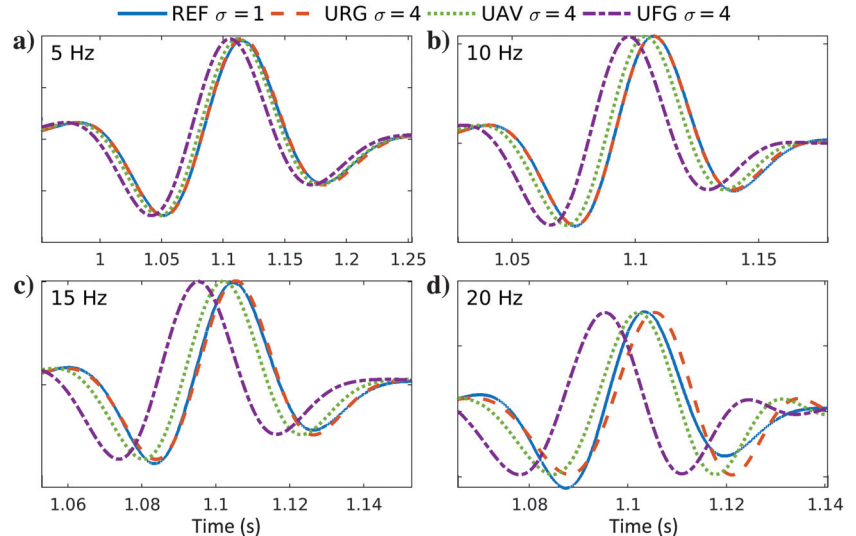


Figure 7. A comparison of traces is obtained for the reference periodic model (REF) and other upscaled models (UAV, UFG, and URG). All traces in each subplot are generated using the same source frequency shown on the top-left corner of each of the panels. Here, the decimation level σ represents the ratio of the number of nodes in a given subdomain to that in the upscaled domain.



we observe, as expected, small errors at low frequencies, with increasing errors in all upscaled models at higher frequencies (up to 15 Hz) and the appearance of amplitude errors at the highest frequencies. It is worth noting that the waveforms computed using the UAV model show significant traveltimes errors at frequencies of 10–20 Hz and phase delays are observed for the URG at high frequencies, whereas the phases are advanced for UAV and UFG.

Reflection geometry

We use a model comprising of three layers, with small-scale heterogeneities present in the second layer. The velocities for the

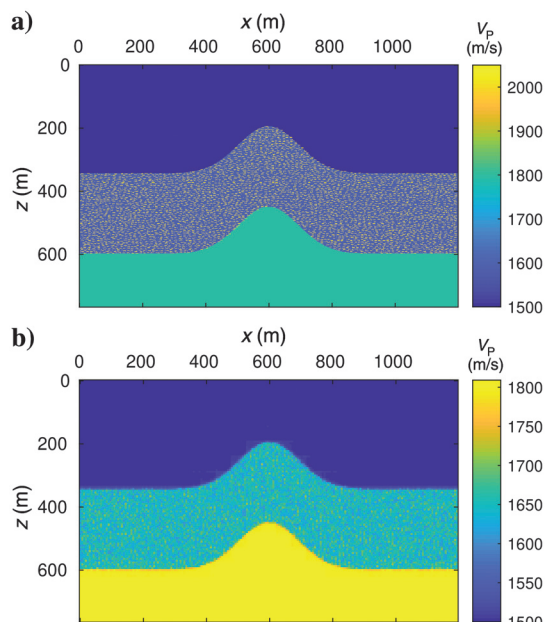


Figure 8. (a) The fine-scale three-layer model with scatterers used as reference model (REF) and (b) the URG model.

layers are [1500, 1600, 1800] m.s⁻¹ in depth-increasing order, as shown in Figure 8. The middle layer in the model has a constant thickness of 300 m, which contains two types of heterogeneities of dimensions (1.5 m × 1.5 m) and (7.5 m × 1.5 m), respectively. The heterogeneities are randomly distributed within the domain and have a finite probability of touching neighboring heterogeneities. Rectangular and square heterogeneities are assigned constant velocities of 2250 and 2200 m.s⁻¹, respectively. We have used 19 shots placed at the surface and at an interval of 40 nodes. Receivers are located at all nodes at the surface (in all the shots). We use a Ricker wavelet with a central frequency of 15 Hz. A comparison of seismograms is shown in Figure 9 for a single shot. The seismogram generated for URG is in good agreement with the waveform obtained for REF. Direct arrivals have been clipped to highlight the reflected phases. The reflected waveforms obtained using URG are slightly delayed in comparison with REF.

These two models are used for comparing the effect of upscaling in RTM (Baysal et al. 1983). It is widely used to generate kinematically accurate subsurface images by crosscorrelating the forward- and reverse-propagating wavefields. The imaging condition used for RTM can be stated as

$$I(x, z) = \sum_s \sum_{\tau} F(x, z, \tau) R(x, z, \tau), \quad (17)$$

where $F(x, z, \tau)$ is the forward-propagating source wavefield, $R(x, z, \tau)$ is the reverse-propagating receiver wavefield at time τ , and s represents the sources/shots.

To carry out the comparison, we first compute the record for 19 shots using the reference model. We then compute the RTM images using these data for the REF and the URG models. The RTM images thus obtained, shown in Figure 10, are nearly identical and show negligible shifts in reflector positions. In this process, we remove the direct arrivals before carrying out the RTM and apply a scaling to enhance the deeper reflector.

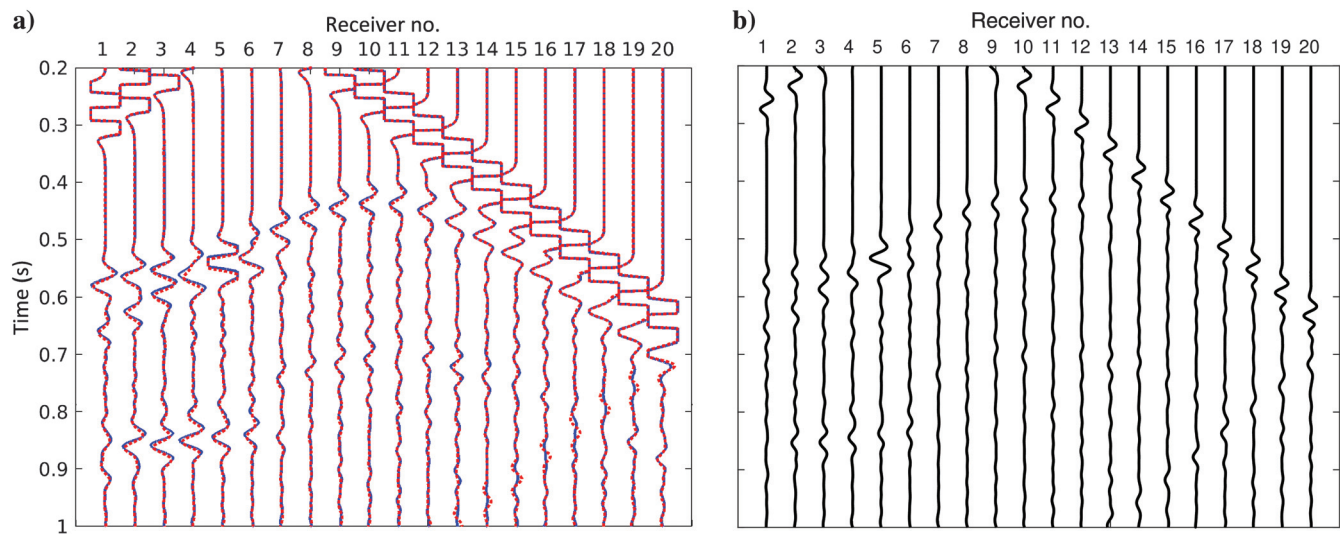


Figure 9. (a) A comparison of the seismogram obtained for three-layer model with scatterers reference model (solid blue line) and its URG model (dotted red line). (b) The difference between these two seismograms at the common-receiver locations.

COMPUTATION TIME

The REF model consists of 1024×512 nodes, and the wave equation is solved for 4000 time steps. The total time taken for a single forward simulation on the REF model is $T_s \approx 116$ s, and the time for carrying out RTM using single shot is $T_r = 386$ s. The computational cost of RTM is higher because it includes time for two forward calculations, crosscorrelation of forward and adjoint wavefields, and input/output from storage.

The simulation time for the upscaled model consists of two parts: first, time spent in upscaling (t_u), and second, time spent in seismic simulation (t_s). Because the upscaling is an “embarrassingly parallel” problem, we can write its total cost as $t_u/N + t_s$, where N is the number of cores used for parallelization. We have carried out upscaling using $\sigma = 4$, which takes about $t_u = 35$ s (estimated for parallel execution) and $t_s = 6$ s. The computation time for RTM using single shot takes about $t_r = 29$ s, which is almost six times faster. In fact, with increasing numbers of shots (N_s), the speedup obtained is even higher, approaching the ratio $T_r/t_r \sim 13$ for a large N :

$$\text{Speedup} = \frac{N_s \times T_r}{t_u/N + N_s \times t_r} = \frac{T_r}{t_u/(N \times N_s) + t_r} \rightarrow \frac{T_r}{t_r}. \quad (18)$$

Upscaling and RTM processes may be seen as the offline and online stages, respectively. The offline stage cost is high, but it helps the online stage to run very efficiently, and in the present case, the overall efficiency increases almost 13 times.

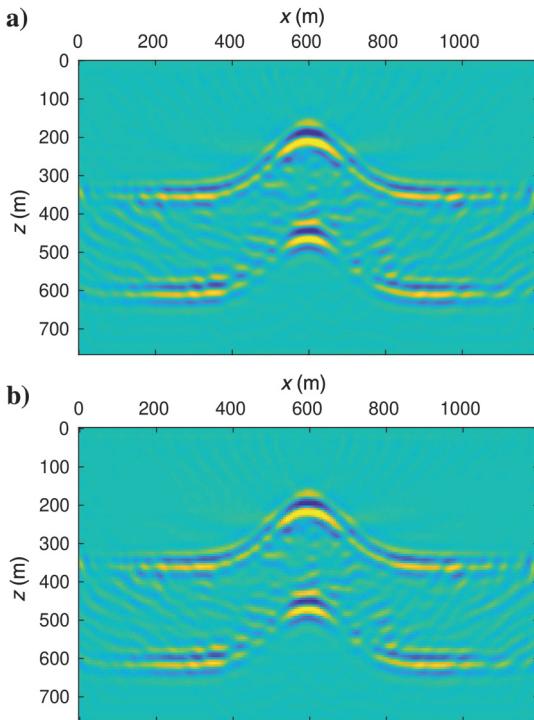


Figure 10. A comparison of RTM images obtained for three-layer model with scatterers using: (a) fine-scale reference model (REF) and (b) upscaled model (URG).

CONCLUSION

We have demonstrated the upscaling of the 2D acoustic wave equation based on RG theory. This requires a modified 2D Fourier operator, decomposing the computational domain into subdomains for avoiding large size multidimensional Fourier operators, and an expansion and truncation technique to mitigate edge effects along the edges of subdomains. We discuss various important characteristics for this scheme, e.g., it honors the wave equation, it is independent of the geometry of the heterogeneity or the layer structure present within the medium, it is free from boundary artifacts, and it does not lower the symmetry of the acoustic wave equation (for the density-invariant case). It is shown that the limit to which upscaling may be carried out is controlled by the property of the numerical-derivative operator, i.e., accuracy and dispersion. We compare the seismograms computed post RG-based upscaling, harmonic averaging, and low-pass filtering. This method reduces the computational cost significantly and makes the upscaling process feasible, even on computer systems with small memory size. At present, the technique has two limitations: (1) it relies on a uniform grid to apply Fourier-based upscaling and blocking process and (2) the determination of the C_H term requires computing the inverse of a matrix (for each block), requiring large computation time, which in turn places constraints on the block size.

ACKNOWLEDGMENTS

The authors thank Shell Global Solutions International, B.V. for supporting this work through funding from CW325423. We would like to thank A. Fitchner and two other anonymous reviewers, the editors of GEOPHYSICS, and M. Sen for their valuable time and comments.

DATA AND MATERIALS AVAILABILITY

Data associated with this research are confidential and cannot be released.

APPENDIX A MODIFIED FOURIER OPERATOR

Consider a 2D function $g(z, x)$ sampled uniformly over a 2D domain using $M \times N$ nodes as $g(i, j) = g(i\Delta h, j\Delta h)$, where $i \in \{1, 2, \dots, N\}$ and $j \in \{1, 2, \dots, M\}$. The conventional 2D Fourier transform for the discrete function is given by $G(u, v) = \mathcal{F}g(i, j)$, and for the discrete case, it may be represented as

$$G_{u,v} = \sum_{m=0}^{M-1} \sum_{n=0}^{N-1} e^{-2\pi i(u/m + v/n)} g_{i,j}, \quad (\text{A-1})$$

and in matrix form as (Van Loan, 1992)

$$\mathbf{G} = \mathbf{F}\mathbf{g}. \quad (\text{A-2})$$

We will modify the Fourier operator \mathbf{F} , such that it yields the response to high and low wavenumbers separately. First, we look into the 2D wavenumber spectrum, $\mathbf{K}(u, v)$ in Figure A-1, and mark the regions for low and high discrete wavenumbers. Here, the lower K and L wavenumbers (user prescribed) represent the lower wavenumbers.

It will produce into four wavenumber-based regions: low-low ($\mathbf{K}_{\bullet,l}^{\bullet}\mathbf{K}_{\bullet,l}^{\bullet}$), low-high ($\mathbf{K}_{\bullet,l}^{\bullet}\mathbf{K}_{\bullet,h}^{\bullet}$), high-low ($\mathbf{K}_{\bullet,h}^{\bullet}\mathbf{K}_{\bullet,l}^{\bullet}$), and high-high ($\mathbf{K}_{\bullet,h}^{\bullet}\mathbf{K}_{\bullet,h}^{\bullet}$). The dot (\bullet) in the subscript represents the axis, and the

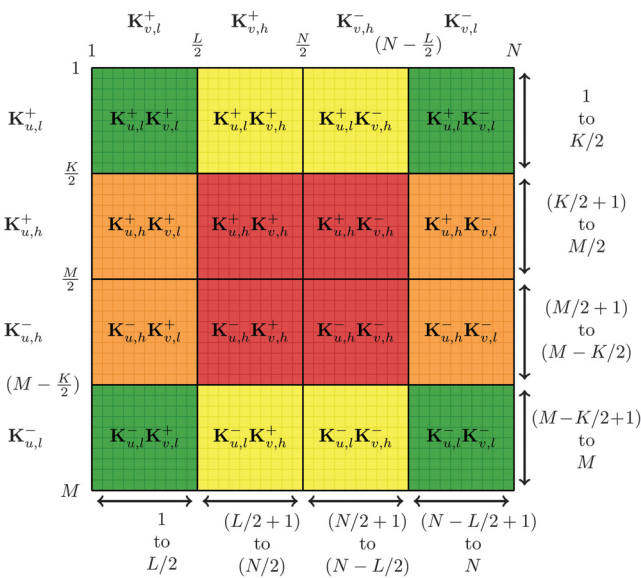


Figure A-1. Distribution of wavenumbers ($\mathbf{K}(u, v)$) obtained for the conventional Fourier transform $G(u, v) = \mathbf{F}g(x, z)$. The total number of discrete wavenumbers along the u, v axes is M, N , of which only the lower K and L wavenumbers along the respective axes are to be retained. Subscripts u and v are used to indicate the associated axes, and h and l represent the high- and low-wavenumber ranges, respectively. Superscripts + and - indicate the positive and negative wavenumbers, respectively.

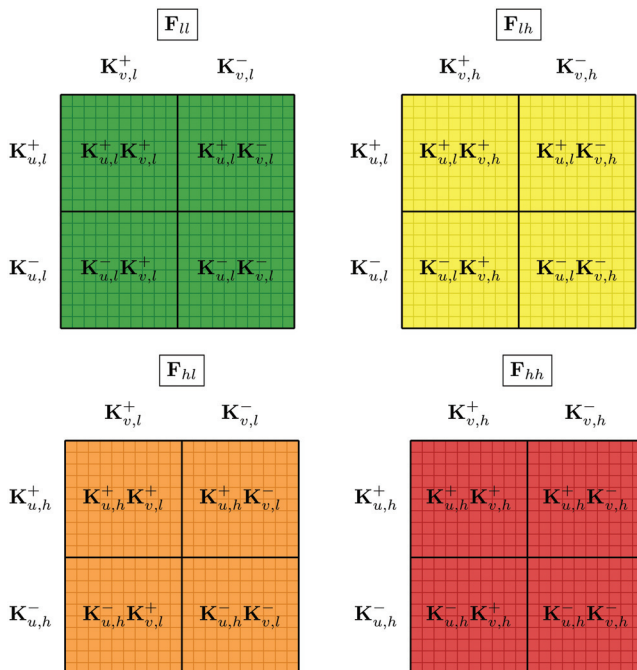


Figure A-2. Distribution of wavenumbers for the different parts of modified Fourier operator, namely, $\mathbf{F}_{ll}, \mathbf{F}_{lh}, \mathbf{F}_{hl}$, and \mathbf{F}_{hh} .

superscript denotes the positive/negative wavenumbers. A combination of wavenumber (positive/negative) and the selected axis (u/v) further divides each aforementioned region, e.g., low-low regions, into four parts. The four wavenumber-based regions are extracted, as shown in Figure A-2, and the corresponding rows of the operator for each region are obtained as $\mathbf{F}_{ll}, \mathbf{F}_{lh}, \mathbf{F}_{hl}$, and \mathbf{F}_{hh} . These four operators are concatenated to form the modified Fourier operator (on the right) and may be succinctly represented (on the left) as

$$\begin{bmatrix} \mathcal{F}_l \\ \mathcal{F}_h \end{bmatrix} = \begin{bmatrix} \mathbf{F}_{ll} \\ \mathbf{F}_{lh} \\ \mathbf{F}_{hl} \\ \mathbf{F}_{hh} \end{bmatrix}. \quad (\text{A-3})$$

In this modified Fourier operator, the first KL rows will correspond to the lower wavenumbers, and the remaining $MN - KL$ rows will correspond to the higher wavenumbers. Once the operator is constructed, the computation of the expression is straightforward

$$\hat{\mathbf{C}}_{ll} = \mathcal{F}_l c^2 \mathcal{F}_l, \quad (\text{A-4})$$

$$\hat{\mathbf{C}}_{lh} = \mathcal{F}_l c^2 \mathcal{F}_h, \quad (\text{A-5})$$

$$\hat{\mathbf{C}}_{hl} = \mathcal{F}_h c^2 \mathcal{F}_l, \quad (\text{A-6})$$

$$\hat{\mathbf{C}}_{hh} = \mathcal{F}_h c^2 \mathcal{F}_h, \quad (\text{A-7})$$

where c is the velocity of the medium, expressed as a diagonal matrix.

REFERENCES

- Andersson, U., B. Engquist, G. Ledfelt, and O. Runborg, 1999, A contribution to wavelet-based subgrid modeling: Applied and Computational Harmonic Analysis, **7**, 151–164, doi: [10.1006/acha.1999.0264](https://doi.org/10.1006/acha.1999.0264).
- Backus, G. E., 1962, Long-wave elastic anisotropy produced by horizontal layering: Journal of Geophysical Research, **67**, 4427–4440, doi: [10.1029/JZ067i011p04427](https://doi.org/10.1029/JZ067i011p04427).
- Baysal, E., D. D. Kosloff, and J. W. Sherwood, 1983, Reverse time migration: Geophysics, **48**, 1514–1524, doi: [10.1190/1.1441434](https://doi.org/10.1190/1.1441434).
- Bensoussan, A., J. Lions, and G. Papanicolaou, 1978, Asymptotic analysis for periodic structures, 1st ed.: North Holland.
- Brisard, S., and L. Dormieux, 2010, FFT-based methods for the mechanics of composites: A general variational framework: Computational Materials Science, **49**, 663–671, doi: [10.1016/j.commatsci.2010.06.009](https://doi.org/10.1016/j.commatsci.2010.06.009).
- Burgos, G., Y. Capdeville, and L. Guillot, 2016, Homogenized moment tensor and the effect of near-field heterogeneities on nonisotropic radiation in nuclear explosion: Journal of Geophysical Research: Solid Earth, **121**, 4366–4389, doi: [10.1002/2015JB012744](https://doi.org/10.1002/2015JB012744).
- Cance, P., and Y. Capdeville, 2015, Validity of the acoustic approximation for elastic waves in heterogeneous media: Geophysics, **80**, no. 4, T161–T173, doi: [10.1190/geo2014-0397.1](https://doi.org/10.1190/geo2014-0397.1).
- Capdeville, Y., M. Zhao, and P. Cupillard, 2015, Fast Fourier homogenization for elastic wave propagation in complex media: Wave Motion, **54**, 170–186, doi: [10.1016/j.wavemoti.2014.12.006](https://doi.org/10.1016/j.wavemoti.2014.12.006).
- Chertock, A., and D. Levy, 2005, On wavelet-based numerical homogenization: Multiscale Modeling & Simulation, **3**, 65–88, doi: [10.1137/030600783](https://doi.org/10.1137/030600783).
- Christie, M. A., 1996, Upscaling for reservoir simulation: Journal of Petroleum Technology, **48**, 1004–1010, doi: [10.2118/37324-JPT](https://doi.org/10.2118/37324-JPT).
- Coppersmith, D., and S. Winograd, 1987, Matrix multiplication via arithmetic progressions: Proceedings of the 19th Annual ACM Symposium on Theory of computing, 1–6.

- Coult, N., 2006, Explicit formulas for wavelet-homogenized coefficients of elliptic operators: *Applied and Computational Harmonic Analysis*, **21**, 360–375, doi: [10.1016/j.acha.2006.04.002](https://doi.org/10.1016/j.acha.2006.04.002).
- Dablain, M. A., 1986, The application of high-order differencing to the scalar wave equation: *Geophysics*, **51**, 54–66, doi: [10.1190/1.1442040](https://doi.org/10.1190/1.1442040).
- De Leon, D., 2008, A new wavelet multigrid method: *Journal of Computational and Applied Mathematics*, **220**, 674–685, doi: [10.1016/j.cam.2007.09.021](https://doi.org/10.1016/j.cam.2007.09.021).
- Dorobantu, M., and B. Engquist, 1998, Wavelet-based numerical homogenization: *SIAM Journal on Numerical Analysis*, **35**, 540–559, doi: [10.1137/S0036142996298880](https://doi.org/10.1137/S0036142996298880).
- Engquist, B., and O. Runborg, 2009, Wavelet-based numerical homogenization, in B. Engquist, A. Fokas, E. Hairer, and A. Iserles, eds., *Highly oscillatory problems*: Cambridge University Press, London Mathematical Society Lecture Note Series, 98–126, doi: [10.1017/CBO9781139107136.006](https://doi.org/10.1017/CBO9781139107136.006).
- Engstrom, C., and D. Sjoberg, 2007, On two numerical methods for homogenization of Maxwell's equations: *Journal of Electromagnetic Waves and Applications*, **21**, 1845–1856.
- Fichtner, A., and S. M. Hanasoge, 2017, Discrete wave equation upscaling: *Geophysical Journal International*, **209**, 353–357, doi: [10.1093/gji/ggx016](https://doi.org/10.1093/gji/ggx016).
- Gao, K., E. T. Chung, R. L. Gibson, S. Fu, and Y. Efendiev, 2015, A numerical homogenization method for heterogeneous, anisotropic elastic media based on multiscale theory: *Geophysics*, **80**, no. 4, D385–D401, doi: [10.1190/geo2014-0363.1](https://doi.org/10.1190/geo2014-0363.1).
- Grechka, V., and M. Kachanov, 2006, Effective elasticity of fractured rocks: A snapshot of the work in progress: *Geophysics*, **71**, no. 6, W45–W58, doi: [10.1190/1.2360212](https://doi.org/10.1190/1.2360212).
- Hanasoge, S., U. Agarwal, K. Tandon, and J. M. V. A. Koelman, 2017, Renormalization group theory outperforms other approaches in statistical comparison between upscaling techniques for porous media: *Physical Review E*, **96**, 033313, doi: [10.1103/PhysRevE.96.033313](https://doi.org/10.1103/PhysRevE.96.033313).
- Hanasoge, S. M., 2016, Spatio-spectral concentration of convolutions: *Journal of Computational Physics*, **313**, 674–686, doi: [10.1016/j.jcp.2016.02.068](https://doi.org/10.1016/j.jcp.2016.02.068).
- Kennett, B. L., and A. Fichtner, 2020, Exploiting seismic waveforms: *Correlation, heterogeneity and inversion*: Cambridge University Press.
- Li, L., J. Tan, D. Zhang, A. Malkoti, I. Abakumov, and Y. Xie, 2021, FDwave3D: A MATLAB solver for the 3D anisotropic wave equation using the finite-difference method: *Computational Geosciences*, **25**, 1565–1578, doi: [10.1007/s10596-021-10060-3](https://doi.org/10.1007/s10596-021-10060-3).
- Malkoti, A., N. Vedanti, and R. K. Tiwari, 2018, An algorithm for fast elastic wave simulation using a vectorized finite difference operator: *Computers & Geosciences*, **116**, 23–31, doi: [10.1016/j.cageo.2018.04.002](https://doi.org/10.1016/j.cageo.2018.04.002).
- Mishra, N., J. Vondrejc, and J. Zeman, 2016, A comparative study on low-memory iterative solvers for FFT-based homogenization of periodic media: *Journal of Computational Physics*, **321**, 151–168, doi: [10.1016/j.jcp.2016.05.041](https://doi.org/10.1016/j.jcp.2016.05.041).
- Moulinec, H., and P. Suquet, 1998, A numerical method for computing the overall response of nonlinear composites with complex microstructure: *Computer Methods in Applied Mechanics and Engineering*, **157**, 69–94, doi: [10.1016/S0045-7825\(97\)00218-1](https://doi.org/10.1016/S0045-7825(97)00218-1).
- Persson, P.-O., and O. Runborg, 2001, Simulation of a waveguide filter using wavelet-based numerical homogenization: *Journal of Computational Physics*, **166**, 361–382, doi: [10.1006/jcph.2000.6662](https://doi.org/10.1006/jcph.2000.6662).
- Schoenberg, M., and F. Muir, 1989, A calculus for finely layered anisotropic media: *Geophysics*, **54**, 581–589, doi: [10.1190/1.1442685](https://doi.org/10.1190/1.1442685).
- Song, X., and T. H. Jordan, 2018, Effective-medium models of inner-core anisotropy: *Journal of Geophysical Research: Solid Earth*, **123**, 5793–5813, doi: [10.1029/2017JB015089](https://doi.org/10.1029/2017JB015089).
- Spetzler, J., and R. Snieder, 2004, The Fresnel volume and transmitted waves: *Geophysics*, **69**, 653–663, doi: [10.1190/1.1759451](https://doi.org/10.1190/1.1759451).
- Van Loan, C., 1992, Computational frameworks for the fast Fourier transform: SIAM.
- Vdovina, T., S. E. Minkoff, and O. Korostyshevskaya, 2005, Operator upscaling for the acoustic wave equation: *Multiscale Modeling & Simulation*, **4**, 1305–1338, doi: [10.1137/050622146](https://doi.org/10.1137/050622146).
- Wang, Y., 2015, Frequencies of the Ricker wavelet: *Geophysics*, **80**, no. 2, A31–A37, doi: [10.1190/geo2014-0441.1](https://doi.org/10.1190/geo2014-0441.1).
- Zijl, W., M. A. N. Hendriks, and C. M. P. 't Hart, 2002, Numerical homogenization of the rigidity tensor in Hooke's law using the node-based finite element method: *Mathematical Geology*, **34**, 291–322, doi: [10.1023/A:1014894923280](https://doi.org/10.1023/A:1014894923280).

Biographies and photographs of the authors are not available.